1

Optical, Photoluminescent, and Photoconductive Properties of Novel High-Performance Organic Semiconductors

Oksana Ostroverkhova, Andrew D. Platt and Whitney E. B. Shepherd
Oregon State University
USA

1. Introduction

Organic semiconductors have been investigated as an alternative to inorganic semiconductors due to their low cost, ease of fabrication, and tunable properties (Forrest, 2004). Applications envisioned for organic semiconductors include xerography, thin-film transistors, light-emitting diodes, solar cells, organic lasers, and many others (Peumans et al., 2003; Murphy & Frechet, 2007; Samuel & Turnbull, 2007). Since most of these applications rely on the conductive and photoconductive properties of the materials, it is important to understand physical mechanisms of charge photogeneration, transport, trapping, and recombination. However, despite numerous theoretical and experimental studies of the optical and electronic properties of organic solids, these mechanisms are not well understood and are still the subject of debate in the literature (Sariciftci, 1997; Podzorov et al., 2004; Moses et al., 2006; Troisi & Orlandi, 2006; Coropceanu et al., 2007; Cheng & Silbey, 2008; Laarhoven et al., 2008). Indeed, it is a complicated task to reveal and utilize the *intrinsic* properties of organic materials, since they are often masked by the influence of impurities, the presence of which is sensitive to the methods of material purification and device fabrication. As a result, measurements performed in the same material using different experimental techniques often provide conflicting results (Nelson et al., 1998; Hegmann et al., 2002; Podzorov et al., 2003; Jurchescu et al., 2004; Lang et al., 2004; Thorsmølle et al., 2004; Ostroverkhova et al., 2005a; Ostroverkhova et al., 2006a; Koeberg et al., 2007; Laarhoven et al., 2008; Najafov et al., 2008; Marciniak et al., 2009). Experimental methods that probe charge carrier dynamics on picosecond (ps) time-scales after a 100-femtosecond (fs) pulsed photoexcitation have had most success in revealing intrinsic properties of organic semiconductors (Hegmann et al., 2002; Thorsmølle et al., 2004; Hegmann et al., 2005; Ostroverkhova et al., 2005a; Ostroverkhova et al., 2005b). In contrast, techniques that probe equilibrium charge transport are much more sensitive to extrinsic effects (Nelson et al., 1998; Knipp et al., 2003; de Boer et al., 2004; Jurchescu et al., 2004). However, since properties under equilibrium conditions are relevant for most devices, it is necessary to understand how they are related to intrinsic properties and find ways to improve materials and device fabrication techniques in order to minimize extrinsic effects. Therefore, one of the emphases of this chapter is on photoexcited charge carrier dynamics from sub-ps (non-equilibrium) to many seconds (equilibrium) after photoexcitation in a variety of organic crystals and thin films (Sections 3.3-3.4).

Source: Advances in Lasers and Electro Optics, Book edited by: Nelson Costa and Adolfo Cartaxo,
ISBN 978-953-307-088-9, pp. 838, April 2010, INTECH, Croatia, downloaded from SCIYO.COM

Of particular technological interest are small-molecular-weight solution-processable materials that can be cast into high-performance (photo)conductive thin films. Functionalized anthradithiophene (ADT) and pentacene derivatives have attracted considerable attention due to their high charge carrier mobility, photoconductivity, and luminescence. In particular, charge carrier (hole) mobilities of over 1.2 cm^2/Vs have been observed in thin-film transistors (TFTs) based on solution-deposited films of these materials (Park et al., 2007; Park et al., 2008). Slight chemical modifications of the side groups of both ADT and pentacene derivatives lead to considerable changes in molecular packing, which affect electronic and optical properties of thin films (Platt et al., 2009a; Platt et al., 2009b; Platt et al., 2009c). Additional changes in these properties may be produced by functionalization of the core of the molecule. In Sections 3.1-3.5, we will summarize optical, photoluminescent (PL), and (photo)conductive properties of several functionalized ADT and pentacene derivatives. In addition to a promising potential of ADT pristine compounds for (opto)electronic applications, the availability of these high-performance, solution-processable, structurally similar, derivatives with different highest occupied molecular orbital (HOMO) and lowest unoccupied molecular orbital (LUMO) energies can be utilized to create composites with optical and electronic properties tailored for specific applications. In Sections 3.1.3 and 3.3.2, we will describe how charge carrier dynamics in ADT films can be manipulated using competition between charge and energy transfer achieved by introducing various guest molecules into an ADT host (Day et al., 2009a). An ultimate understanding of the charge carrier and exciton dynamics in organic semiconductors can be reached, however, only if relationships between charge transfer and energy transfer rates on the molecular level and macroscopic (photo) conductivity in the bulk material are established. Our preliminary studies of properties of individual molecules are presented in Section 3.2.

Finally, most devices that utilize (opto) electronic properties of materials require application of static electric fields with deposited electrodes. The processes occurring at the metal-organic interfaces at the electrodes can significantly affect the performance of a device (Brutting, 2005; Day et al., 2009b), introducing another difficulty in the materials characterization and another variable into the device performance. Effects of the electrode material on the (photo)conductive performance of organic thin-film devices, at various time-scales after photoexcitation, will be briefly reviewed in Section 3.6.

2. Experimental

2.1 Materials and sample preparation

In our studies of non-equilibrium charge carrier dynamics at sub-ps time scales after 100-fs photoexcitation (Section 3.3.1), we used single crystals of ultra-high-purity pentacene (Pc) (Jurchescu et al., 2004), pentacene derivative functionalized with 6,13-bis (triisopropylsilylethynyl) (TIPS) side groups (TIPS-pentacene) (Hegmann et al., 2002; Ostroverkhova et al., 2005a; Ostroverkhova et al., 2005b; Anthony, 2006; Ostroverkhova et al., 2006a), rubrene (Rub) (Podzorov et al., 2003; Podzorov et al., 2004), and tetracene (Tc) (Moses et al., 2006) (Fig.1). The Pc powder was purified using vacuum sublimation under a temperature gradient (Jurchescu et al., 2004). Rub, Tc and Pc single crystals were obtained using physical vapor transport techniques as described in Jurchescu et al., 2004 and Podzorov et al., 2003. The TIPS-pentacene single crystals were grown in a saturated tetrahydrofuran (THF) solution at 4°C (Anthony et al., 2001). Eight TIPS-pentacene crystals

and four Pc, Rub and Tc crystals (each) were used in these experiments and yielded similar results (Ostroverkhova et al., 2006a). For the same experiments, we also prepared polycrystalline Pc and TIPS-pentacene thin films. All of the Pc and some TIPS-pentacene films were prepared on mica, glass, or KCl substrates by thermal evaporation of the corresponding powder heated to 200–250 °C in high vacuum (10^{-6}–10^{-7} Torr) at a deposition rate of 0.3 Å/ s. The thickness of the films was measured with a profilometer (Tencor Instruments) and ranged between 150 nm and 1.3 μm (Ostroverkhova et al., 2005a; Ostroverkhova et al., 2005b). TIPS-pentacene films drop-cast from THF solution at room temperature were also prepared.

In our studies of anisotropy of the transient photoconductivity (Section 3.3.1), we used single crystals of pentacene functionalized with: (i) TIPS and (ii) 6,13-bis (triethylsilylethynyl) (TES) side groups. The single crystals had dimensions typically around (1.5-2) mm x (2-4) mm (as illustrated in Fig.9(c)) with a thickness of 300-500 μm. Although both TIPS-pentacene and TES-pentacene crystals are triclinic (with the unit cell parameters listed in Table 1), the molecular packing and resulting π-overlap in these crystals is different, as the TIPS-pentacene crystals assume a more two-dimensional (2D) "brick-wall"-type structure, while the TES-pentacene crystals exhibit a one-dimensional (1D) "slipped-stack"-type structure (Figs.9(a) and (b), respectively)(Anthony, 2006). Our crystallographic analysis showed that the largest area crystal surface corresponds to the *a*-*b* plane of the crystals, with the *a*-axis parallel (||) to the long axis in both TIPS-pentacene and TES-pentacene crystals. TIPS-pentacene and TES-pentacene crystals have almost identical absorption spectra in solution, with the absorption edge at around 700 nm, which shifts to ~850 nm in a crystal. Eight TIPS and four TES crystals were used in these experiments (Ostroverkhova et al., 2006b).

Compound	a (Å)	b (Å)	c (Å)	α (deg)	β (deg)	γ (deg)
TIPS-pent.	7.565	7.75	16.835	89.15	78.42	83.63
TES-pent.	7.204	9.994	11.326	80.81	89.13	82.21
ADT-TES-F	7.71	7.32	16.35	87.72	89.99	71.94
ADT-TIPS-F	7.58	8.18	16.15	100.85	92.62	98.79

Table 1. Unit cell parameters for functionalized pentacene and ADT derivatives used in our studies.

In our studies of photophysical and photoconductive properties on time-scales from sub-nanoseconds (ns) after 100 fs excitation to an equilibrium (Sections 3.1, 3.3.2, 3.4, and 3.5), we explored thin films of TIPS-pentacene, of fluorinated ADT derivatives functionalized with TES and TIPS side groups (ADT-TES-F and ADT-TIPS-F, respectively), and of another ADT derivative functionalized with TIPS side-groups, ADT-TIPS-CN (Figure 1) (Day et al., 2008; Day et al., 2009a; Day et al., 2009b; Platt et al., 2009b). In addition to pristine materials, we explored films of ADT-TES-F doped with various concentrations of C_{60}, TIPS-pentacene, or ADT-TIPS-CN. Stock solutions of functionalized ADT derivatives were prepared at ~ 1% by weight in toluene. For solution measurements, solutions were prepared by dilution of stock solutions to ~10^{-4} M. Films with thickness of 1 − 2 μm were prepared by drop-casting stock solutions onto glass substrates at ~60 °C. Composite films were similarly prepared

from stock solutions of known mixtures of ADT-TES-F and C_{60}, TIPS-pentacene, or ADT-TIPS-CN. When dealing with pristine compounds, this preparation method yielded polycrystalline ADT-TES-F, ADT-TIPS-F, and TIPS-pentacene and amorphous ADT-TIPS-CN films (as confirmed by X-ray diffraction and transmission electron microscopy (TEM)). The unit cell parameters for the fluorinated ADT derivatives studied are listed in Table 1. For measurements of dark current and photoresponse, glass substrates were prepared by photolithographic deposition of either 5 nm/50 nm-thick Cr/Au or 100 nm-thick aluminum (Al) electrode pairs. Each pair consisted of 10 interdigitated finger pairs, with 1 mm finger length, 25 μm finger width and 25 μm gaps between the fingers of opposite electrodes. Films were drop-cast onto the interdigitated regions. Films on coplanar electrodes with 25 or 50 μm gap were also prepared.

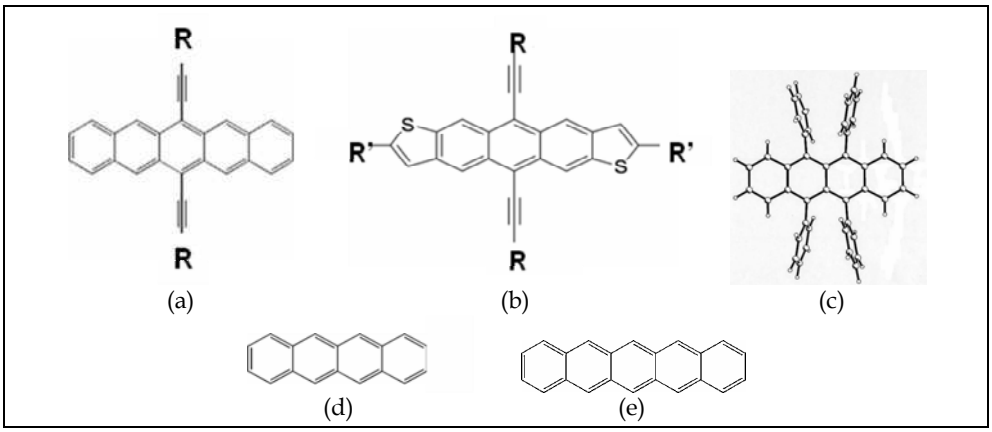

Fig. 1. Molecular structures of (a) functionalized pentacene, (b) functionalized ADT, (c) rubrene (Rub), (d) tetracene (Tc), and (e) pentacene (Pc). R = TIPS or TES, R' = F or CN.

2.2 Measurements of optical and photophysical properties

Optical absorption spectra were measured using a halogen lamp and a fiber-coupled Ocean Optics USB2000 spectrometer. Absorbance A was calculated from the incident (I_0) and transmitted (I) beam intensities as $A = -\mathrm{Log}(I/I_0)$. Reflection losses were taken into account by referencing with respect to cuvettes with pure solvent or clean glass substrates for solution and film measurements, respectively. Emission spectra were acquired in a custom fluorescence measurement setup with laser excitation at wavelengths of either 400 nm (frequency-doubled mode-locked Ti:Sapphire laser from KM Labs) or 532 nm (Nd:YVO_4 laser from Coherent, Inc.). Emitted photons were collected using a parabolic mirror and detected with a fiber coupled spectrometer (Ocean Optics USB2000 calibrated against a 3100 K black-body emitter). Absorption of solutions was measured using a standard 1 cm path length quartz cuvette with a halogen light source fiber-optically delivered to the sample holder and spectrometer. Photoluminescence (PL) quantum yields (QYs) in solution were referenced against standards with known quantum yields and corrected for differences in optical density and solvent refractive index. The ADT derivatives were measured against rhodamine 6G in ethanol ($\Phi = 0.95$) and DCDHF-N-6 in toluene ($\Phi = 0.85$) (Lord et al., 2007). The QY of TIPS pentacene solution was measured against rhodamine 6G in ethanol and

Alexa Fluor 647 in a phosphate buffer solution (pH 7.2, Φ = 0.33). The QYs in films were estimated using DCDHF-N-6 in polymethylmethacrylate (PMMA) (Φ = 0.98) as a reference and assuming a value of 1.7 for the index of refraction (Lord et al., 2007). The detection limit of the setup was estimated to be at $\Phi \approx 0.5\%$ at 650 nm.

PL lifetime measurements were performed using a mode-locked Ti:Sapphire laser frequency-doubled with a beta-barium borate (BBO) crystal with a repetition rate of 93 MHz picked at 9.3 MHz using a home-built pulse picker (based on a TeO_2 acousto-optic modulator from NEOS) and 80-fs pulses as the excitation source. A single-photon avalanche photodiode (SPAD – Molecular Photonic Devices) was used in conjunction with a time-correlated single-photon counter (TCSPC) data analysis board (PicoQuant TimeHarp 200) for detection. The instrument response function (IRF) (~200 ps) was recorded using scattered light from an etched microscope slide. For measurements of the temperature dependence of film spectra, samples on pre-cut microscope slides were mounted on a custom built electrically heated and water cooled stage (range: 278 − 360 K) for temperature control. PL measurements were taken in situ over the entire temperature range, in ambient air. Similar experiments were previously performed under N_2 atmosphere and showed no discernable difference.

For measurements of electric field-induced PL quenching, either 532 nm cw light or pulsed 400 nm light was focused on the samples similar to those used in our (photo)conductivity studies. At 532 nm cw photoexcitation, PL was collected using a Thorlabs amplified photodetector and a SRS830 lock-in amplifier. Keithley 237 source-measure unit was used to apply voltage in the range of 0-500 V and measure photocurrent, simultaneously with measurements of the PL. At 400 nm pulsed excitation, PL transient decay was detected using SPAD and TCSPC, as described above. The experiment was repeated at voltages up to 500 V and at different temperatures.

2.3 Single-molecule-level PL imaging

Samples for PL imaging at the single-molecule level (Section 3.2) were prepared from stock solutions of 1% by weight PMMA (75,000 m.w.) in toluene. ADT-TES-F was doped into the solution at the level of 10^{-10} per PMMA molecule. This solution was then spun coat onto clean glass coverslips at 2000 rpm for 55 s. The samples were imaged with an Olympus IX71 inverted microscope with a 100X UPlanApo objective under wide-field 532 nm cw illumination. The PL was detected by an Andor iXon DU-897 EMCCD camera.

2.4 Transient photocurrent measurements

2.4.1 Optical-pump-terahertz (THz) probe spectroscopy

A detailed description of the optical-pump – THz-probe experimental setup can be found in Lui & Hegmann, 2001. Briefly, an amplified Ti:Sapphire laser source (800 nm, 100 fs, 1 kHz) was used to produce optical pump pulses at wavelengths of 400-800 nm through various wave-mixing schemes and THz probe pulses generated via optical rectification in a 0.5 mm-thick ZnTe crystal. The samples were mounted on 1-2 mm apertures, and both the THz probe and optical pump pulses were at normal incidence to the surface of the films (*a*-*b* plane) of the single crystal samples. The room-temperature data were taken in air. For temperature dependence measurements, the samples were mounted in an optical cryostat (sample in vapor). The electric field of the THz pulse transmitted through the samples, $T(t)$, was detected by free-space electro-optic sampling in a 2-mm-thick ZnTe crystal and

monitored at various delay times (Δt) with respect to the optical pump pulse. The range of optical pump fluences was 0.9-1.5 mJ/cm². No transient photoconductivity was observed upon optical excitation of the substrates alone. Optical excitation of all thin film and single crystal samples resulted in a change in the transmitted electric field (-ΔT(t)) due to the transient photoconductivity (i.e. *mobile* photogenerated carriers) (Hegmann et al., 2002; Hegmann et al., 2005; Ostroverkhova et al., 2005a; Ostroverkhova et al., 2005b; Ostroverkhova et al., 2006a; Ostroverkhova et al., 2006b). In the absence of the phase shift between THz waveforms obtained in the unexcited and optically excited sample, as was the case for all our samples, the optically induced relative change in the THz peak amplitude (-(T-T_0)/T_0≡ -ΔT/T_0, where T_0 is the amplitude of the THz pulse transmitted through unexcited sample) provides a direct measure of the transient photoconductivity (Hegmann et al., 2002; Thorsmølle et al., 2004; Ostroverkhova et al., 2005a). The time resolution of this experimental setup was ~400 fs. In the approximation of a thin conducting film on an insulating substrate, the differential transmission (-ΔT/T_0) due to optical excitation of mobile carriers at small |ΔT/T_0| is related to the transient photoconductivity as follows (Lui and Hegmann, 2001; Hegmann et al., 2002; Thorsmølle et al., 2004):

$$\sigma = -(\Delta T/T_0)(1+N)/(Z_0 L), \tag{1}$$

where Z_0 = 377 Ω is the impedance of free space, N is the refractive index of the substrate at THz frequencies, and L is the film thickness. Using this expression, and setting the maximum value for the transient response at Δt = 0 so that $|\Delta T/T_0|_{MAX} = |\Delta T(0)/T_0|$, the product of the charge carrier mobility (μ) and photogeneration efficiency (η) can be calculated as follows (Hegmann et al., 2002; Ostroverkhova et al., 2005a; Ostroverkhova et al., 2005b):

$$\mu\eta = \left|\frac{\Delta T(0)}{T_0}\right| \frac{h\nu(1+N)}{eF(1-R)(1-\exp[-\alpha L])Z_0}, \tag{2}$$

where e is the electric charge, h is Planck's constant, ν is the light frequency, α is the absorption coefficient, F is the incident fluence, and R is the reflection coefficient.

2.4.2 Direct measurements of fast photocurrent using digital sampling oscilloscope

For transient photoconductivity measurements on sub-100 ps to hundreds of microsecond (μs) time-scales after pulsed photoexcitation, an amplified Ti:Sapphire laser (800 nm, 100 fs, 1 kHz) was used in conjunction with a frequency-doubling beta-barium borate (BBO) crystal to excite the samples. Voltage was supplied by a Keithley 237 source-measure unit, and light pulse-induced transient photocurrent was measured with a 50 Ω load by a 50 GHz CSA8200 digital sampling oscilloscope (DSO). The time resolution of this setup was 30-40 ps.

From the peak of the transient photocurrent ($I_{ph,max}$), a product of charge carrier mobility μ and photogeneration efficiency η was calculated using

$$\mu\eta = I_{ph,max}/(eN_{ph}Ed), \tag{3}$$

where N_{ph} is the number density of absorbed photons per pulse, E is the static electric field ($E = V/L$, where V is the applied voltage and L is the gap between the electrodes), e is the charge of the electron, and d is the channel width.

2.5 Dark current and cw photocurrent measurements

For dark current and cw photocurrent measurements, the samples were embedded in a fixture incorporating a thermoelectric unit for temperature control (range: 285−350 K). The Keithley 237 source-measure unit was used to measure current through the sample in the absence and in the presence of cw photoexcitation with a Nd:YVO_4 laser at 532 nm. The photocurrent was calculated as the difference between the two.

2.6 Scanning photocurrent microscopy

Scanning photocurrent microscopy has been previously utilized in probing internal electric field distributions, mapping electronic band structure, measuring mobility-lifetime products, etc. in inorganic and organic films, nanowires, carbon nanotubes, and graphene sheets (Gu et al., 2006; Agostinelli et al., 2007; Ahn et al., 2007; Park et al., 2009). In our experiments, ADT films on coplanar electrodes, either Al or Au, separated by a 50-μm gap, were excited with a focused beam from the glass substrate side, and photoresponse was monitored as the excitation spot was moved across the gap from one electrode to another (Day et al., 2009), under applied voltage. This experiment was performed with either pulsed 100-fs 400-nm excitation or cw 532-nm excitation, using laser sources described above. In the case of pulsed excitation, a lens with 2.5-cm focal distance was used to focus the beam with pulse energy of ~1 nJ to an approximately 4-μm spot at the sample. The lens was translated along the gap using a micrometer-controlled translation stage. At each position of the lens, transient photocurrent resulting from excitation of a localized region of the film was recorded with the DSO. In the case of cw excitation, the sample was placed on an Olympus IX-71 inverted microscope, and a 10x objective with a numerical aperture of 0.6 was used to focus the beam at a power of ~0.4 μW to an approximately 400-nm spot. Position of the localized excitation with respect to the electrodes was monitored by a CCD camera that detected fluorescence (emitted by the photoexcited region of the sample) collected through the same objective. The sample was translated using a closed-loop piezoelectrically controlled x-y stage with sub-nm resolution, with a speed of 1 μm/s. Cw light was chopped at 565 Hz, and the amplitude of the modulated photocurrent signal was measured by a Stanford Research Systems 830 lock-in amplifier. The experiment was repeated as a function of applied voltage and light power, as well as at different voltage polarities, directions of the scan, and lengths of the waiting period between successive scans.

3. Results

3.1 Optical properties

3.1.1 Dilute solutions

Figure 2 shows optical and PL properties of functionalized ADT and pentacene derivatives in toluene solution. In all spectra, vibronic progression due to coupling of the electronic state to ring-breathing vibrational modes (~1400 cm^{-1}), characteristic of oligoacenes, is observed (Pope & Swenberg, 1999). In solutions, optical properties were determined primarily by the core of the molecule and were not affected by TIPS or TES side-groups, which resulted in identical spectra of, for example, ADT-TES-F and ADT-TIPS-F in Fig. 2 or TIPS- and TES-pentacene (only TIPS-pentacene data are shown). Spectra of ADT-TIPS-CN and TIPS-pentacene in solution were both red-shifted with respect to those of ADT-TIPS(TES)-F. Small Stokes shifts of <10 nm, observed in all solutions, are due to rigidity of the molecular core of oligoacenes. PL lifetime decay of solutions was well described by a single-exponential

function (~exp[−t/τ], where τ is the PL lifetime). ADT-TIPS-F and ADT-TES-F derivatives exhibited similar lifetimes (τ) of ~9 ns and high PL quantum yields (QYs) (Φ) of ~70% in toluene. Solutions of ADT-TIPS-CN and TIPS-pentacene showed longer lifetimes (~12-12.5 ns) and QYs ~75% (Table 2) (Platt et al., 2009a; Platt et al., 2009b; Platt et al., 2009c).

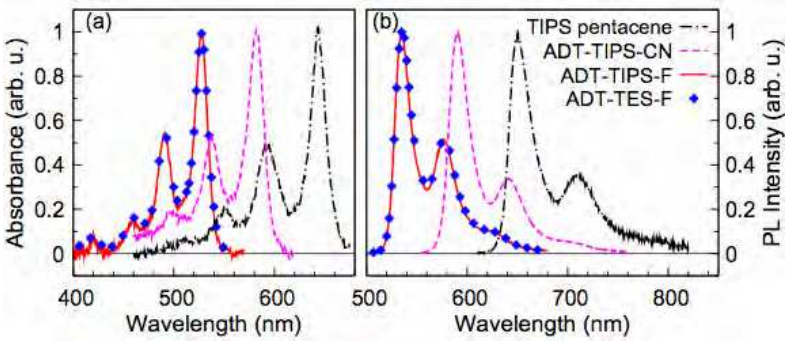

Fig. 2. Normalized optical absorption (a) and PL (b) spectra of functionalized pentacene and ADT derivatives in toluene solution. Spectra of ADT-TES-F and ADT-TIPS-F in solutions are identical. Reprinted from Platt et al., 2009b, with permission. Copyright American Chemical Society (2009).

3.1.2 Thin films

Optical absorption spectra of films (Fig. 3(a)) exhibited a redshift, or displacement Δ, with respect to those in solutions, due to enhanced Coulomb interaction of the molecule with its surrounding and exchange interaction between translationally equivalent molecules (Ostroverkhova et al., 2005b). In general, Δ depends on the molecular-orbital overlap and on the structure and morphology of the film. In contrast to identical absorption and PL spectra of ADT-TIPS-F and ADT-TES-F in solution, those of corresponding films were considerably different (Fig. 3), which we attribute to differences in packing of these molecules in the solid and in film crystallinity. In particular, ADT-TIPS-F and ADT-TES-F films exhibited displacements Δ of ~320 cm^{-1} and ~760 cm^{-1}, respectively. Although Δ exhibited sample-to-sample variation, it was always larger in ADT-TES-F films compared to films of ADT-TIPS-F, indicative of a higher degree of exciton delocalization in ADT-TES-F films. Also redshifted were PL spectra of ADT-TES-F with respect to those of ADT-TIPS-F films (Fig. 3(b)). Vibronic bands in both absorption and PL spectra were broader in films, as compared to solutions, with relative intensities of the bands varied depending on the film thickness and morphology (Platt et al., 2009a; Platt et al., 2009b). Regardless of the film thickness, ADT-TIPS-F films showed a more pronounced vibronic structure of the PL spectra than ADT-TES-F or ADT-TIPS-CN. The differences observed in PL spectra of films compared to those in solutions are due to intermolecular interactions leading to a formation of crystallites and molecular aggregates (whose properties depend on the degree of molecular order, size, and intermolecular coupling). This is further supported by our observations that the PL spectra of molecules under study embedded at low concentrations in the PMMA matrix yielded spectra identical to those of solutions in Fig. 1(b), as expected from non-interacting molecules (Platt et al., 2009b). Although all materials studied could be prone to aggregate formation due to their π-stacking properties, PL properties of aggregates significantly

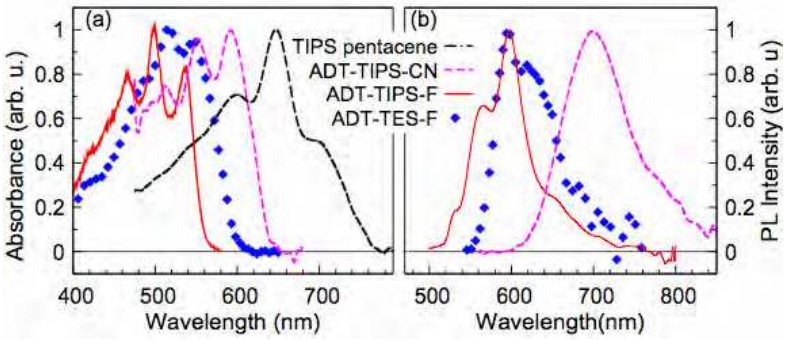

Fig. 3. Normalized optical absorption (a) and PL (b) spectra in TIPS-pentacene and ADT films. No PL response was observed in TIPS-pentacene films. Reprinted from Platt et al., 2009b, with permission. Copyright American Chemical Society (2009).

depended on the material. For example, at room temperature, thin films of ADT-TIPS-F and ADT-TES-F were highly luminescent, with PL QYs reaching 40 − 50% depending on the film thickness and morphology. (These values represent a lower limit, since effects of self-absorption were significant in even the thinnest of our films). In contrast, PL in TIPS-pentacene films was so low that it could not be detected (QYs of < 0.5%).

In all materials studied, the PL decay dynamics in films were faster than those in solutions and could be described by a bi-exponential function ($\sim a_1 \exp[-t/\tau_1] + a_2 \exp[-t/\tau_2]$, where $\tau_{1(2)}$ and $a_{1(2)}$ are shorter (longer) lifetimes and their relative amplitudes, respectively, and $a_1 + a_2 = 1$), characteristic of molecular aggregates. Both τ_1 and τ_2 were shorter than lifetimes τ measured in solutions of the same molecules, and the weighted average lifetimes in films, $\tau_{av} = a_1\tau_1 + a_2\tau_2$, were typically on the order of 0.4 − 4 ns at room temperature, depending on the material, and varied with film quality (e.g. from 1.1 to 2.5 ns in ADT-TIPS-F films).

Temperature dependence. In all ADT films, the PL response was strongly temperature dependent, and PL quantum yields decreased by a factor of 3−6 as the temperature increased from 5 °C to 80 °C, depending on the sample. Figure 4 (a) shows (i) PL QY calculated from the integrated PL spectrum measured at 400 nm excitation, (ii) the peak PL intensity measured under pulsed 80 fs 400 nm excitation with the time resolution of ~ 200 ps, and (iii) integrated time-resolved fluorescence decay measured under pulsed 80 fs 400 nm excitation, all normalized by their values at room temperature of 20 °C, as a function of temperature in an ADT-TIPS-F film. Considerable temperature dependence of the peak PL intensity suggests significant contribution of processes occurring on sub-200 ps time scales, not resolved in our experiments, to the overall temperature dependence of the QYs. The remaining contribution is due to processes occurring on time scales of <2-4 ns. Since no temperature dependence of PL emission of our molecules in solution was observed, the strong temperature dependence observed in films is due to temperature-dependent intermolecular interactions in films (Platt et al., 2009b). In order to quantify the observed temperature dependence, we consider PL quantum yield to be inversely proportional to a sum of temperature independent radiative rate and thermally activated non-radiative rate, so that

$$1/\Phi \sim 1 + a \exp[-\Delta_{PL}/k_B T] , \quad (4)$$

where k_B is the Boltzmann constant, T is temperature, and *a* is a fitting parameter related to the ratio between radiative and temperature-independent non-radiative rate prefactor. PL quenching activation energies Δ_{PL}, obtained from fits of data to Eq.(4) yielded values between 0.11 and 0.27 eV, depending on the sample and on the material (e.g. 0.15 eV in an ADT-TIPS-CN film in Fig.4(b)) (Platt et al., 2009b).

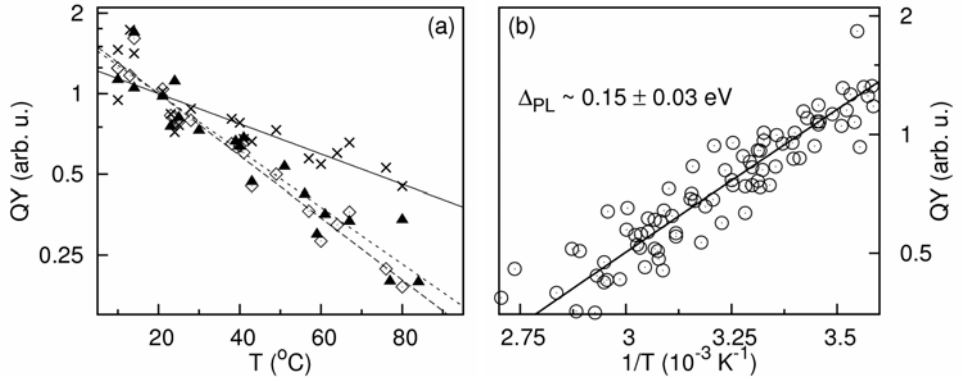

Fig. 4. (a) Temperature dependence of (i) the QYs calculated from the integrated PL spectrum measured at 400 nm excitation (triangles), (ii) peak amplitude of the PL transient measured under pulsed 80 fs 400 nm excitation with 200 ps resolution (×), and (iii) integrated PL decays measured under pulsed 80 fs 400 nm excitation (diamonds) in ADT-TES-F film. All are normalized by their values at room temperature of 20 °C.
(b) Temperature dependence of the QY, normalized at its value at room temperature, obtaine in an ADT-TIPS-CN film. The fit of the QY by Eq. (4) is also shown. Reprinted from Platt et al., 2009b, with permission. Copyright American Chemical Society (2009).

Compound	HOMO[a] (eV)	LUMO[a] (eV)	λ_{abs}[b] (nm)	λ_{PL}[b] (nm)	Φ[c]	τ[c] (ns)	$\lambda_{abs,film}$[d] (nm)	$\lambda_{PL,film}$[d] (nm)
ADT-TES-F	-5.35	-3.05	528	536	0.70	9.4	550	595
ADT-TIPS-F	-5.35	-3.05	528	536	0.72	9.1	537	600
ADT-TIPS-CN	-5.55	-3.49	582	590	0.76	12.7	592	~688
TIPS-pent.	-5.16	-3.35	643	650	0.75	11.8	~705	--

Table 2. Electrochemical and photophysical properties of TIPS-pentacene and ADT derivatives.
[a] Measured using differential pulse voltammetry (Platt et al., 2009b)
[b] Wavelengths of maximal absorption or PL corresponding to 0→0 transitions in toluene solutions
[c] PL QY and PL lifetime in toluene solutions
[d] Wavelengths of maximal absorption or PL in thin films. PL from TIPS-pentacene films could not be detected (QY<0.5%)

Electric field dependence. In order to address a possibility of electric field-induced dissociation of the radiative state, we measured PL spectra and lifetimes upon either cw 532

nm or pulsed 80 fs 400 nm photoexcitation of ADT films, under applied voltage. No changes in the PL QYs, peak PL intensity, or PL lifetimes have been detected at the applied voltages of 0-500 V, i.e., up to average electric fields of 2×10^5 V/cm, at any temperature in the range of 5-80 °C.

3.1.3 Composite thin films

Figure 5 shows absorption and PL spectra of the composite films containing ADT-TES-F host molecules and 2 wt% C_{60}, 10 wt% of TIPS-pentacene or 10 wt% of ADT-TIPS-CN guest molecules. Based on the absorption spectra in Fig. 5(a)), no ground state charge transfer occurs upon addition of guest molecules at these concentrations. In contrast to absorption spectra, addition of any guest molecules to ADT-TES-F in film produced a dramatic effect on the PL spectra (Fig. 5(b)), due to photoinduced charge or energy transfer, depending on the guest (Day et al., 2009a). In particular, very strong photoinduced energy transfer was observed in ADT-TES-F/ADT-TIPS-CN composites: even at a concentration of ADT-TIPS-CN in ADT-TES-F as low as 0.1%, almost no PL emission was observed from the ADT-TES-F host, and the PL response of the film was dominated by that of the ADT-TIPS-CN guest molecules (Platt et al., 2009c). In contrast, photoinduced charge transfer, leading to the PL quenching, is more favored in ADT-TES-F/C_{60} and ADT-TES-F/TIPS-pentacene composites. As we discuss in Section 3.3.2, PL properties of the composites are correlated with photoconductive properties of the same samples on short time-scales after a pulsed 80 fs photoexcitation.

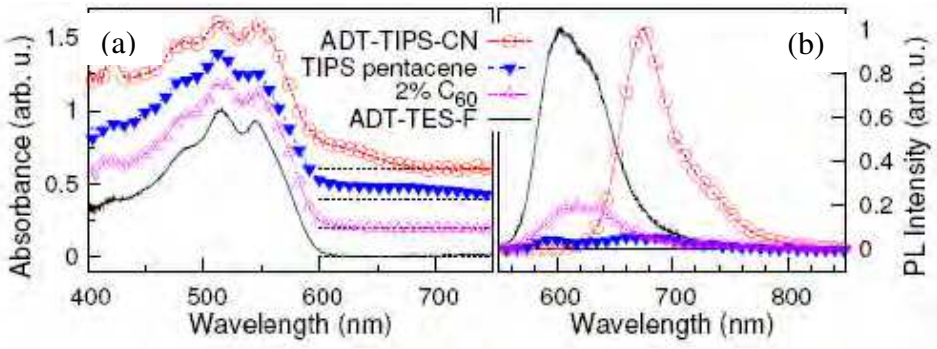

Fig. 5. Optical absorption (a) and PL (b) spectra of a pristine ADT-TES-F film and composites ADT-TES-F/C_{60} (2%), ADT-TES-F/TIPS-pentacene (10%), and ADT-TES-F/ADT-TIPS-CN (10%). Absorption spectra are shifted along y-axis for clarity. Reprinted from Day et al., 2009a, with permission. Copyright American Institute of Physics (2009).

3.2 Properties of individual molecules

Figure 6 shows a typical time trajectory of the PL photon count obtained from an individual ADT-TES-F molecule in a PMMA matrix, as confirmed by a single-step photobleaching at time t = 32 s. This demonstrates that PL quantum yields and photostablity of ADT-TES-F molecules are good enough to enable imaging at the single molecule level at room temperature. Signal–to–noise ratios of over 20:1 were obtained at moderate excitation levels at 532 nm in the epi-illumination geometry. Moreover, ADT-TES-F exhibited remarkably good stability as a single molecule fluorophore, comparable to DCDHF-N-6, which is

currently one of the best fluorophores utilized in single-molecule fluorescence spectroscopy. This opens up new possibilities to study charge- and energy-transfer processes in these materials at nanoscales, which are currently underway in our laboratory.

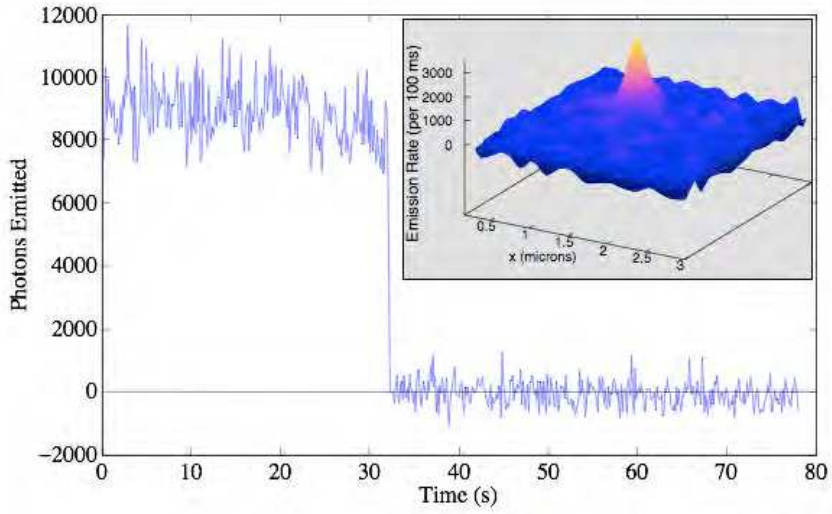

Fig. 6. Time trace of the fluorescence of a single molecule of ADT-TES-F under 700 μW wide-field 532 nm cw illumination. Single-step photobleaching at ~32 s confirms that the trace belongs to a single-molecule. Inset shows a surface plot of the emission of the same molecule with cubic interpolation. Integration time was 100 ms.

3.3 Transient photoconductivity

3.3.1 Non-contract measurements on 400 fs-1 ns time-scales using optical pump-THz probe spectroscopy

Figure 7(a) illustrates the differential THz transmission ($-\Delta T/T_0$) under optical excitation at 580 nm as a function of delay time (Δt) between the optical pump and THz probe pulses, obtained in Pc, TIPS-pentacene, Rub and Tc crystals and Pc and TIPS-pentacene thin films (Ostroverkhova et al., 2005a; Ostroverkhova et al., 2005b; Ostroverkhova et al., 2006a). All transients, except that for the Tc, which was taken at 10 K, were measured at room temperature in air. The onset of the photoresponse reveals a fast photogeneration process for mobile carriers with characteristic times below ~400 fs limited by the time resolution of our setup in all samples. This suggests that free carriers, and not only excitons, can be created in these materials fast, and in the absence of applied electric field. At room temperature (RT), measurements of the peak value of $-\Delta T/T_0$ yielded $\mu\eta$ values (calculated from Eq.(2)) of ~ 0.3-0.35, 0.15-0.2, 0.05-0.06, and 0.03 cm²/(Vs) for Pc, TIPS-pentacene, Rub and Tc crystals, respectively, and 0.02-0.03 and 0.01-0.06 in Pc and TIPS-pentacene thin films, depending on their structure. These values (in particular the photogeneration efficiency η) include initial carrier trapping and recombination occurring within 400 fs after photoexcitation, not resolved in our experiment. If we assume $\eta = 1$, then these $\mu\eta$ values provide a *lower estimate* for the carrier mobility μ. Since $\eta < 1$, the mobility value is higher.

Likewise, if we assume that RT intrinsic mobilities in these materials are on the order of <10 cm^2/Vs in TIPS-pentacene and Tc and ~20-30 $cm^2/(Vs)$ in Rub and Pc (Jurchescu et al., 2004; Podzorov et al., 2004), then the lower limit for the photogeneration efficiency in single crystals is ~1-2% in Pc and TIPS-pentacene and ~0.3% in Rub and Tc. The observed difference in $\mu\eta$ could be due to the differences in: (i) *intrinsic* carrier mobility, (ii) *initial* photogenerated free carrier yield, and (iii) carrier loss due to charge trapping and recombination. Factor (iii) is likely not to be a significant contributor at such short time-scales after photoexcitation. This is supported by our observation of the $\mu\eta$ values measured in good-quality TIPS-pentacene thin films reaching 30 - 40% of those obtained in TIPS-pentacene single crystals, in spite of the abundance of deep traps at the grain boundaries in thin films (Ostroverkhova et al., 2005b). Therefore, the differences in the trapping properties of TIPS-pentacene, Pc, Rub and Tc crystals most likely account only for a factor up to ~2 in the differences in $\mu\eta$ values obtained in these crystals at RT, while further differences are due to factors (i) and (ii). For example, the lower transient photoconductivity observed in Rub compared to Pc single crystals at RT at 400 nm could be mostly due to the lower photogeneration efficiency η (factor (ii)) in Rub, in qualitative agreement with Podzorov et al., 2004 and Lang et al., 2004.

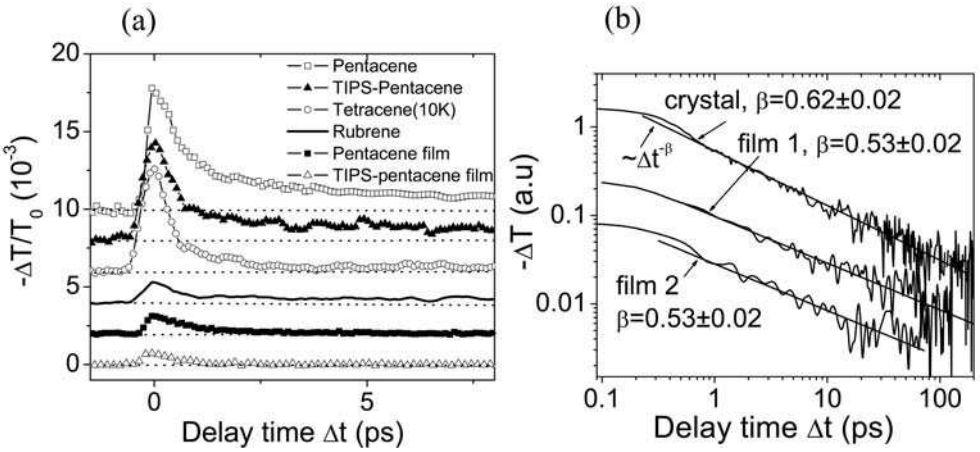

Fig. 7. (a) Differential THz transmission due to transient photoconductivity in various organic crystals and thin films as a function of pump-probe delay time. (b) Decay dynamics of the transient photoconductivity in TIPS-pentacene crystal and two films. Fits with a power-law function are also shown. Adapted from Ostroverkhova et al., 2005b and Ostroverkhova et al., 2006a, with permission. Copyright American Institute of Physics (2005, 2006).

The decay dynamics of the transient photoconductivity yield information about the nature of charge transport, trapping and recombination (Etemad et al., 1981; Moses et al., 1987; Yu et al., 1990). In TIPS-pentacene crystals, the transient photoconductivity exhibited a fast initial decay during the first few picoseconds, followed by a slow decay best described by a power law function ($\sim\Delta t^{-\beta}$) with β= 0.5-0.7 over many orders of magnitude in time, which has been attributed to dispersive transport (Fig.7(b)) (Etemad et al., 1981; Hegmann et al., 2002). Interestingly, these dynamics in TIPS-pentacene crystals did not change appreciably

over a wide temperature range of 5-300 K, which suggests tunneling, rather than thermally-activated hopping, mechanism of charge transport. Similar decay dynamics was observed in Pc crystals at RT and in best TIPS-pentacene films (Ostroverkhova et al., 2005b; Ostroverkhova et al., 2006a). In contrast, photoconductivity in lower-quality TIPS-pentacene and Pc films exhibited fast bi- or single-exponential decay dynamics (~exp[$-\Delta t/\tau_c$]) with time constants τ_c~1 ps for both materials, independent of the temperature, most likely due to deep-level traps at the interfaces between crystallites.

Wavelength dependence. In order to gain insight into the photogeneration process, we repeated the optical pump-THz probe experiment at various pump wavelengths in TIPS-pentacene crystals and Pc and TIPS-pentacene thin films. Due to the short temporal width of the optical pulses (~100 fs), the illumination is not monochromatic, as illustrated in Fig. 8(a), which shows the spectra of some of the optical pump pulses utilized in this experiment. Typical optical absorption spectra of the thin film and single crystal samples are shown in Fig. 8(b). No transient photoresponse was obtained from TIPS-pentacene and Pc thin films upon excitation at 800 nm – the spectral region in which there is too little absorption (Fig. 8(b)). At all wavelengths of optical excitation *within* the absorption spectra, we observed a photoinduced change in THz transmission with a fast onset and decay dynamics similar to that shown in Fig. 7 in all our samples.

Furthermore, $\mu\eta$ calculated from our data was wavelength-independent within our experimental error, as shown in Fig. 8(c). Wavelength-independent photocarrier generation has also been observed in other organic semiconductors using ultrafast techniques (Moses et al., 2000). However, conventional steady-state photoconductivity measurements typically exhibit wavelength-dependent mobile carrier photogeneration efficiencies (Silinsh & Capec, 1994; Pope & Swenberg, 1999), as reported for pentacene single crystals (Lang et al., 2004).

Temperature dependence. The temperature dependence of the photoresponse provides valuable information about the mechanism of photoconductivity (Moses, 1989; Karl, 2001; Karl, 2003). In both single crystals and thin films, the transient photoconductivity *increased* as the temperature *decreased*, as demonstrated in Fig. 8(d). As the temperature *decreased* from 297 K to about 20 K, $\mu\eta$ *increased* in all crystals by a factor of 3-10, depending on the crystal. Assuming η does not increase as the temperature decreases, we can attribute the temperature dependence of $\mu\eta$ shown in Fig. 8(d) to band-like charge carrier transport (Hegmann et al., 2002; Thorsmølle et al., 2004; Ostroverkhova et al., 2005a; Ostroverkhova et al., 2005b), which has not been previously observed over such a *wide* temperature range in Tc and Rub single crystals (de Boer et al., 2004; Newman et al., 2004; Podzorov et al., 2004). The initial increase of $\mu\eta$ by a factor of 1.5 - 3 (depending on the crystal) as the temperature is lowered from 297 K to about 150 K (Fig.8(d)) is consistent with the increase in charge carrier mobility observed from field-effect measurements in Rub (Podzorov et al., 2004) and from space-charge-limited-current measurements in Pc (Jurchescu et al., 2004) and Tc (de Boer et al., 2004) single crystals over the same temperature range. In films, the μη increased from ~0.02 $cm^2/(Vs)$ to ~0.07 $cm^2/(Vs)$ as the temperature decreased from 297 K to 5 K, the trend which has not been previously observed in polyacene thin films. In addition, even though such band-like mobility has been obtained in several organic crystals (Moses, 1989; Karl, 2001; Hegmann et al., 2002; Karl, 2003; de Boer et al., 2004; Jurchescu et al., 2004; Podzorov et al., 2004; Thorsmølle et al., 2004), only a few studies reported the band-like behavior over a wide temperature range (Karl, 2001; Hegmann et al., 2002; Karl, 2003; Thorsmølle et al., 2004), as observed in our experiments (Fig.8). The thin film data in Fig.

8(d) can be fitted with the power law function $\mu\eta \sim T^{-n}$, with the exponent n~0.32, similar to n~0.27 reported from transient photoconductivity measurements of Pc single crystals. (Thorsmølle et al., 2004).

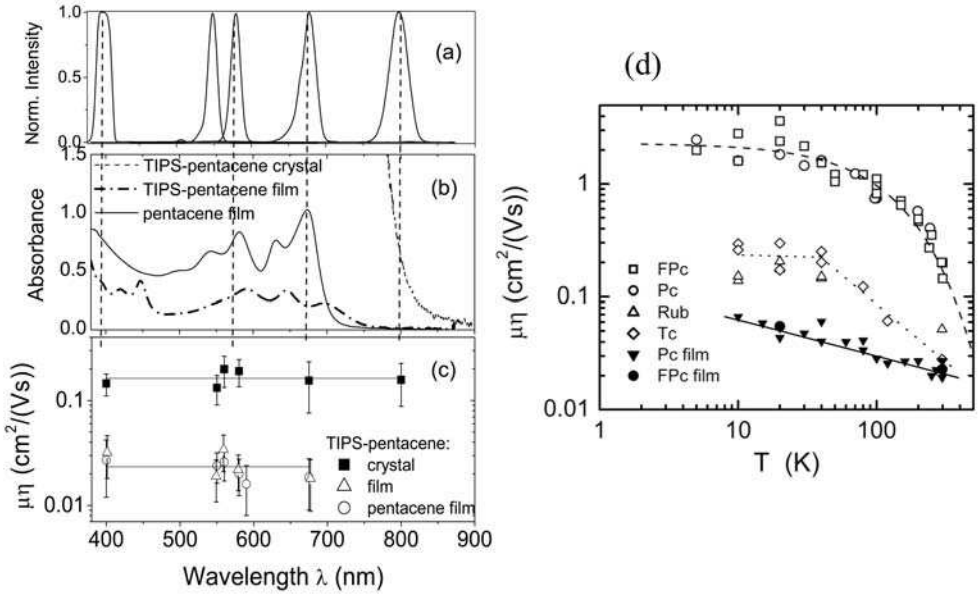

Fig. 8. (a) Normalized intensity spectra of selected optical pump pulses. Spectra of pulses centered at 550 and 590 nm are not included for clarity. (b) Absorption spectra of a TIPS-pentacene crystal and TIPS-pentacene and Pc thin-film samples. (c) Product of mobility and photogeneration efficiency (μη) measured in a TIPS-pentacene crystal and TIPS-pentacene and Pc thin-film samples at room temperature. (d) Temperature dependence of the μη obtained in Pc, Rub, Tc, and TIPS-pentacene (the latter labeled as FPc on the figure) single crystals and Pc and TIPS-pentacene (labeled as FPc) films. Adapted from Ostroverkhova et al., 2005a and Ostroverkhova et al., 2006a, with permission. Copyright American Physical Society (2005) and American Institute of Physics (2006).

Photoconductivity anisotropy. In order to probe the effect of molecular packing on the transient photoconductivity, we performed optical pump-THz probe experiments in TIPS-pentacene and TES-pentacene single crystals (Fig.9(a)-(c)) (Ostroverkhova et al., 2006b). The $-\Delta T/T_0$ transients observed in both TIPS-pentacene and TES-pentacene crystals had very similar shapes and exhibited sub-picosecond charge photogeneration and power-law decay dynamics discussed above (Fig.7). The μη product, calculated using Eq.(2) from the peak of the $-\Delta T/T_0$ transient obtained with both the electric field of the THz probe pulse (E_{THz}) and that of the optical pump pulse (E_{pump}) parallel to the *a*-axis, yielded ~0.15-0.2 cm²/(Vs) and ~0.05-0.06 cm²/(Vs) for the charge carrier mobility in TIPS-pentacene and TES-pentacene crystals, respectively, depending on the sample. As discussed above, these numbers represent lower limits for the charge carrier mobility along the *a*-axis. The triclinic symmetry group of TIPS-pentacene and TES-pentacene crystals (Table 1) leads to a complex picture of charge transport described by six components of the mobility tensor μ_{ij}, where i,j = *x, y, z*,

are components in an orthogonal coordinate system (choice of which is somewhat arbitrary), and $\mu_{ij}=\mu_{ji}$. In general, the principal axes of the mobility tensor do not coincide with the crystallographic axes, are different for hole and electron transport, and are temperature-dependent (Karl, 2001). In order to measure charge carrier mobility anisotropy, separately from that of the photogeneration efficiency, we performed the following experiments (Ostroverkhova et al., 2006b). The crystal was rotated in the azimuthal (*a*-*b*) plane, so that the angle (φ) between the direction of E_{THz} and the *a*-axis of the crystal changed (at $\varphi = 0^o$ E_{THz} was parallel to the *a*-axis). The polarization of the pump (E_{pump}) was rotated with the crystal using a half-wave plate and a polarizer combination in order to maintain E_{pump} parallel to the *a*-axis and ensure the same fluence at all angles. At every angle, the peak value of $-\Delta T/T_0$ was measured and the $\mu\eta$ product was calculated using Eq.(2). In this case, the observed angular dependence of the photoconductivity was purely due to that of the charge carrier mobility, and not due to the combined effects of the mobility and photogeneration efficiency anisotropy. Figures 9 (d) and (e) show the angular dependence of the charge carrier mobility (averaged over all samples measured at 800-nm, 400-nm and 580-nm-excitation) normalized to the value at $\varphi = 0^o$ in TIPS-pentacene and TES-pentacene crystals, respectively. The charge carrier mobility along a certain direction $\boldsymbol{l}=(l_i, l_j, l_k)$ is given by $\mu_{II} = \mu_{ij}l_il_j$. For convenience, we chose the orthogonal coordinate system (x,y,z) so that x || *a*-axis, $y \perp x$ and is in the *a*-*b* plane, and $z \perp a$-*b* plane. Then, in the *a*-*b* plane, $\boldsymbol{l}$ = (cosφ, sinφ, 0), and the mobility along $\boldsymbol{l}$ is:

$$\mu_{II} = \mu_{xx} (\cos\varphi)^2 + \mu_{yy} (\sin\varphi)^2 + \mu_{xy} \sin(2\varphi) \quad (5)$$

For example, the mobility along the *a*-axis is $\mu_{aa}= \mu_{xx}$. The equation above normalized by μ_{xx} was used to fit the data in Fig. 9 (d) and (e) and yielded $\mu_{yy}/\mu_{xx} = 0.34 \pm 0.05$ (0.09±0.05) and $\mu_{xy}/\mu_{xx} = -0.17 \pm 0.04$ (0.06±0.04) in TIPS-pentacene (TES-pentacene). Using these components and substituting $\varphi = \gamma$ from Table 1 (for μ_{bb}) in Eq.(5), we obtained the ratio of the mobilities along *a*- and *b*-axis (μ_{aa}/μ_{bb} = 3.2 and 8 in TIPS-pentacene and TES-pentacene, respectively). Assuming that μ_{yz} and μ_{xz} components of the mobility tensor are small, we diagonalized the *x*-*y* part of the tensor and determine the directions of the principal axes 1 and 2, as well as the corresponding mobilities μ_{11} ($1.04\mu_{aa}$ and $1.004\mu_{aa}$ in TIPS-pentacene and TES-pentacene, respectively) and μ_{22} ($0.30\mu_{aa}$ and $0.086\mu_{aa}$ in TIPS-pentacene and TES-pentacene, respectively), whose ratio μ_{22}/μ_{11} yielded 3.5 ± 0.6 and 12 ± 6 for TIPS-pentacene and TES-pentacene, respectively. The mobility anisotropy of 3.5 in the TIPS-pentacene crystal is very similar to that obtained in Rub and Pc single crystals using a field-effect transistor geometry (Podzorov et al., 2004). Considerable difference in the in-plane mobility anisotropy between the TIPS-pentacene and TES-pentacene crystals supports a theoretical prediction of much stronger mobility anisotropy in the case of the TES-pentacene-type crystals that favor 1D charge transport based on the crystal structure and molecular packing (Figs.9(a) and (b)). In TIPS-pentacene, the principal axes 1 and 2 constitute angles $\varphi_1 = -14^o$ and $\varphi_2 = 76^o$ with respect to the *a*-axis, respectively (Fig.9(d)). Interestingly, the highest mobility axis does not exactly coincide with the direction of maximum π-overlap along the *a*-axis, which highlights the contribution of factors unrelated to band structure, such as fluctuations of the intermolecular coupling, to charge carrier mobility in organic molecular crystals. In TES-pentacene, the principal (highest mobility) axis 1 is coincident with the direction of maximum π-overlap along the *a*-axis (Figs. 9(b) and (e)). However, it is possible

that due to the above mentioned fluctuations in intermolecular electronic coupling, the observed in-plane anisotropy of ~12 is smaller than that expected based solely on the band structure. The observed mobility anisotropy in these samples, which is one of the signatures of band-like charge transport in organic crystals, further supports the occurrence of band-like transport in functionalized pentacene single crystals.

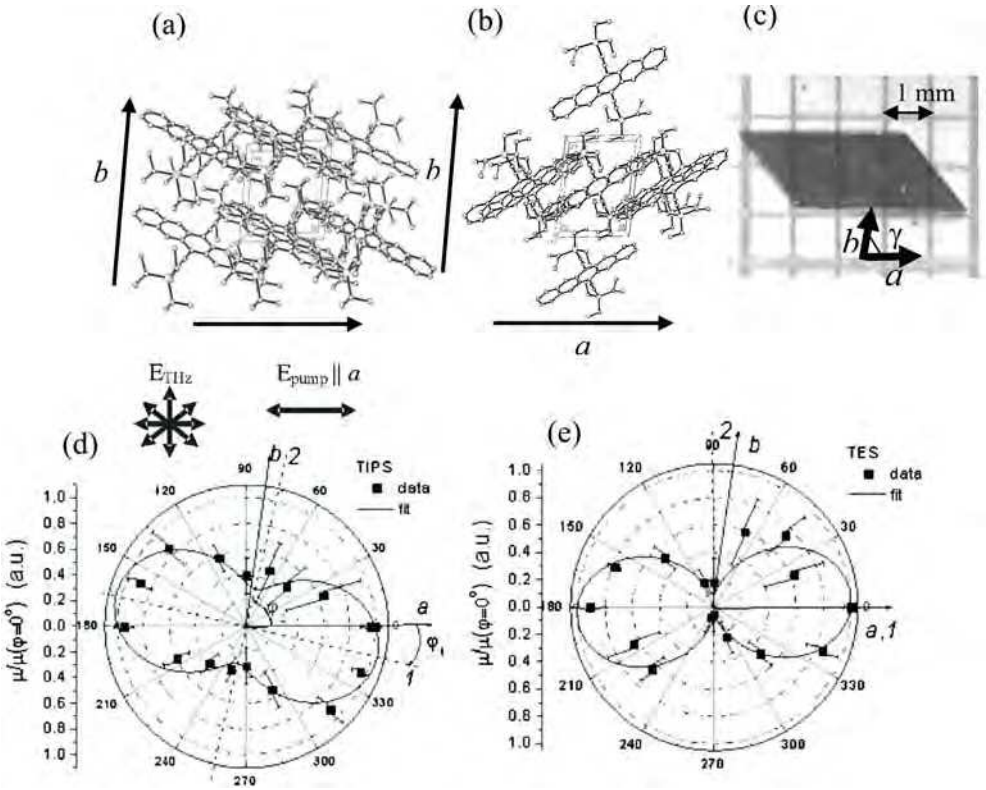

Fig. 9. Molecular packing in (a) TIPS-pentacene and (b) TES-pentacene crystals. (c) Typical TIPS-pentacene crystal. Dependence of the charge carrier mobility on the azimuthal angle φ obtained in (d) TIPS-pentacene and (e) TES-pentacene crystals. In both crystals, φ=0° corresponds to the *a* axis. Lines correspond to the fit with a function described in the text. Crystallographic *a* and *b* axes as well as the principal axes 1 and 2 are also shown. Adapted from Ostroverkhova et al., 2006b, with permission. Copyright American Institute of Physics (2006).

3.3.2 Transient photocurrent on 30 ps to 1 ms time-scales in thin-film device structures

Pristine Materials. Upon excitation with 400 nm 100 fs pulses under applied voltage, thin-film devices based on TIPS-pentacene and ADT derivatives (ADT-TES-F and ADT-TIPS-F, Section 3.1) showed fast photoresponse, with the rise time of 30-40 ps, limited by the time resolution of the sample fixture and DSO, which supports our earlier observations (using noncontact optical pump-THz probe techniques, Section 3.3.1) of fast charge carrier